Materials Science & Engineering A 804 (2021) 140739

Contents lists available at ScienceDirect

Materials Science & Engineering A

journal homepage: http://www.elsevier.com/locate/msea

Short communication

Dynamic precipitation of σ-phase and element partitioning in equiatomic CoCrFeMnNi high-entropy alloy

Unhae Lee [a], Boris Straumal [b], Nokeun Park [c,d,*]

[a] POSCO Technical Research Laboratories, Gwangyang, 57807, Republic of Korea
[b] Institute of Solid State Physics and Chernogolovka Scientific Center of the Russian Academy of Sciences, Chernogolovka, 142432, Russia
[c] School of Materials Science and Engineering, Yeungnam University, 280 Daehak-ro, Gyeongbuk, 38541, Republic of Korea
[d] Institute of Materials Technology, Yeungnam University, 280 Daehak-ro, Gyeongbuk, 38541, Republic of Korea

ARTICLE INFO

Keywords:
Dynamic precipitation
σ-phase
Element partitioning
Dynamic recrystallization
High-entropy alloy

ABSTRACT

We studied the development and element partitioning for σ-phase precipitation during hot compression of the CoCrFeMnNi HEA. The σ-phase mainly observed in the necklaced area (NA), where dynamic recrystallization (DRX) occurred but did not occur in the deformed area (DA). The σ-phase increases the hardness and elastic modulus measured by nanoindentation in NA, compared to that of DA. Several defects are transferred by the interface reaction of the crystal grains accompanied by the partitioning of the Cr and Ni elements. This results in the accelerated dynamic precipitation of the Cr-rich σ-phase.

1. Introduction

Recently, several studies have investigated high-entropy alloys (HEAs). While carbon steels or light alloys usually consist of one major component and, occasionally, up to seven alloying elements, HEAs do not have a main component and consist of more than five elements at relatively equal concentrations [1–3]. The equiatomic CoCrFeMoNi HEA known as the Cantor alloy has the face-centered cubic (FCC) single-phase structure [1]. The alloy shows increased ductility and yield strength as the temperature decreases to that of liquid nitrogen. The temperature also affects other properties of the alloy such as corrosion resistance, fatigue, and wear resistance [4–10].

Grain refinement has shown promise for increasing the strength and ductility of HEAs [6,11–13]. Otto et al. [6] studied the tensile properties of the CoCrFeMnNi HEA between 77 and 1073 K. It was found that the yield strength and ultimate tensile strength increased dramatically as the deformation temperature decreased, and the highest strength was observed for the smallest grain size. Static recrystallization through the annealing process after high strain can help to obtain fine grains. Moreover, the grain size decreases with increasing amount of cold deformation and lower annealing temperature [14–17].

Schuh et al. [4] studied the mechanical properties and microstructure changes during the annealing process after high-pressure torsion (HPT) of the CoCrFeMnNi HEA. They found that the alloy was single-phase FCC for the annealing temperatures above 800 °C, while the σ-phase precipitated upon annealing at temperatures below 800 °C. Using experiments and thermodynamic calculations, Park et al. [18] reported that the Cr-rich σ-phase occurs after HPT and annealing process in the CoCrFeMnNi HEA. The σ-phase formation in the FCC structure can serve as another strengthening mechanism [4,18–22].

Otto et al. [5] observed σ-phases with sizes of approximately 10–20 μm when annealing was performed at 700 °C for 500 days. Pickering et al. [23] observed σ-phases sized approximately 2–5 μm from the microstructure image obtained after annealing for 500 h at the same temperature. Park et al. [18] heat-treated the CoCrFeMnNi HEA at 700 °C after HPT and observed σ-phase particles sized approximately 100 nm after 10 min. After 60 min, the size of the σ-phase was confirmed to be 100–300 nm. Otto et al. found that the composition of the σ-phase was 46.5% Cr-6.6% Ni such that sufficient diffusion of Cr occurred. Park et al. determined that the Cr content of the σ-phase was relatively low at approximately 25% Cr–15% Ni. This implies that the growth of the σ-phase accompanies the diffusion of Cr. Additionally, these studies indicated that σ-phase precipitation was activated due to high deformation followed by annealing, implying that the deformation is related to σ-phase formation. However, the effect of deformation on the dynamic precipitation of σ-phase, which differs from the static precipitation of the σ-phase investigated in previous studies, is unclear. Therefore, this study aims to understand the development and element

* Corresponding author. School of Materials Science and Engineering, Yeungnam University, 280 Daehak-ro, Gyeongbuk, 38541, Republic of Korea.
E-mail addresses: uhlee@posco.com (U. Lee), nokeun_park@yu.ac.kr (N. Park).

https://doi.org/10.1016/j.msea.2021.140739
Received 11 September 2020; Received in revised form 16 December 2020; Accepted 29 December 2020
Available online 5 January 2021

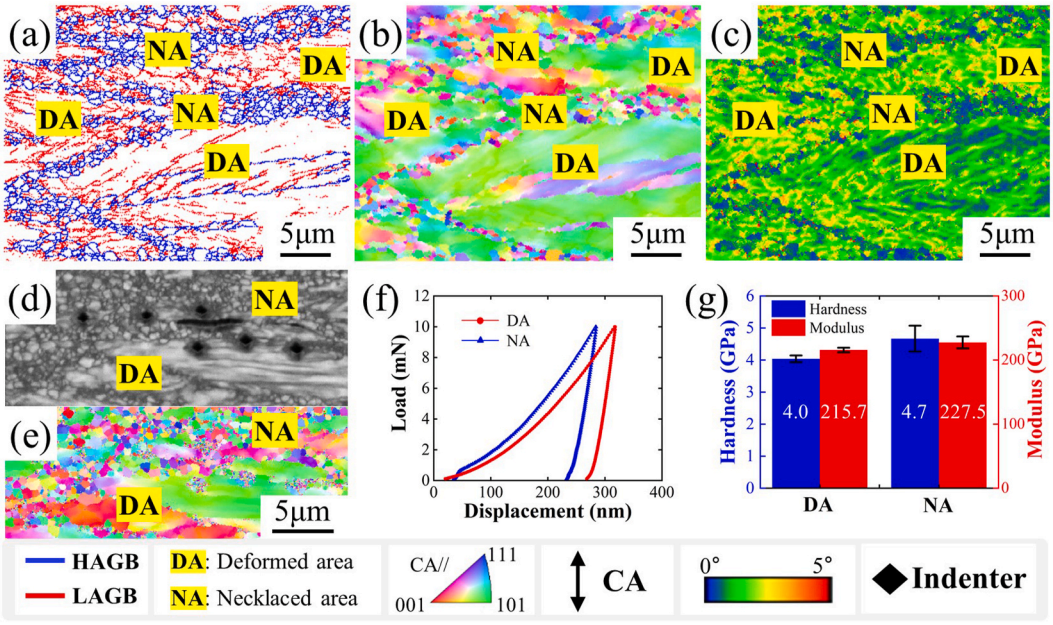

Fig. 1. The microstructures of 70 % compressed sample shown by (a) boundary map, (b) inverse pole figure (IPF) map, and (c) kernel average misorientation (KAM) map of electron backscatter diffraction (EBSD). In (a), blue and red lines indicate high-angle grain boundaries (HAGB), for which the angle is higher than 15°, and low-angle grain boundaries (LAGB), for which the angle is between 2 and 15°, respectively. Deformed area (DA) indicates the deformed initial microstructure and necklaced area (NA) shows the newly developed fine equiaxed grains near the initial grain boundaries. (d) Image quality (IQ) map and (e) IPF map show the nanoindenter locations having the DA and NA. (f) Load-displacement curves measured by nanoindentation in the DA and NA. The average hardness and elastic modulus of DA and NA are shown in (g). (For interpretation of the references to colour in this figure legend, the reader is referred to the Web version of this article.)

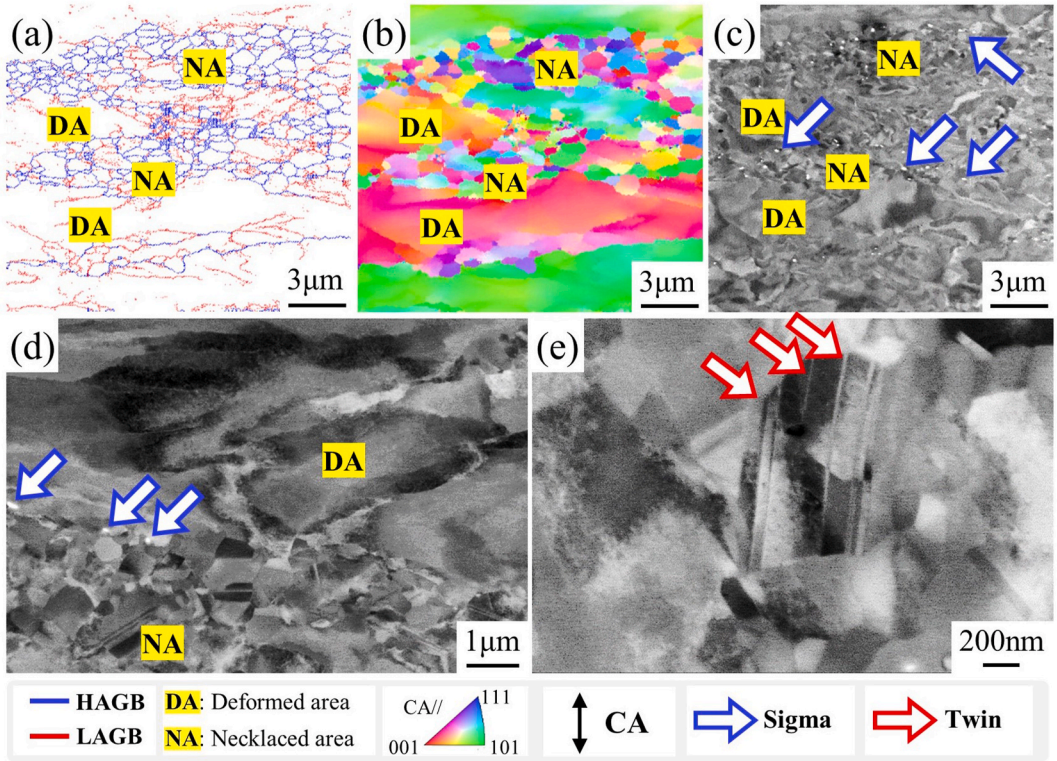

Fig. 2. Interface between NA and DA shown by the boundary map (a), IPF map (b), and electron channeling contrast imaging (ECCI) analysis (c). A magnified view of the interface is shown in (d), and a magnified view of the single fine equiaxed grain is shown in (e). Blue and red arrows indicate σ-phases and twins, respectively. (For interpretation of the references to colour in this figure legend, the reader is referred to the Web version of this article.)

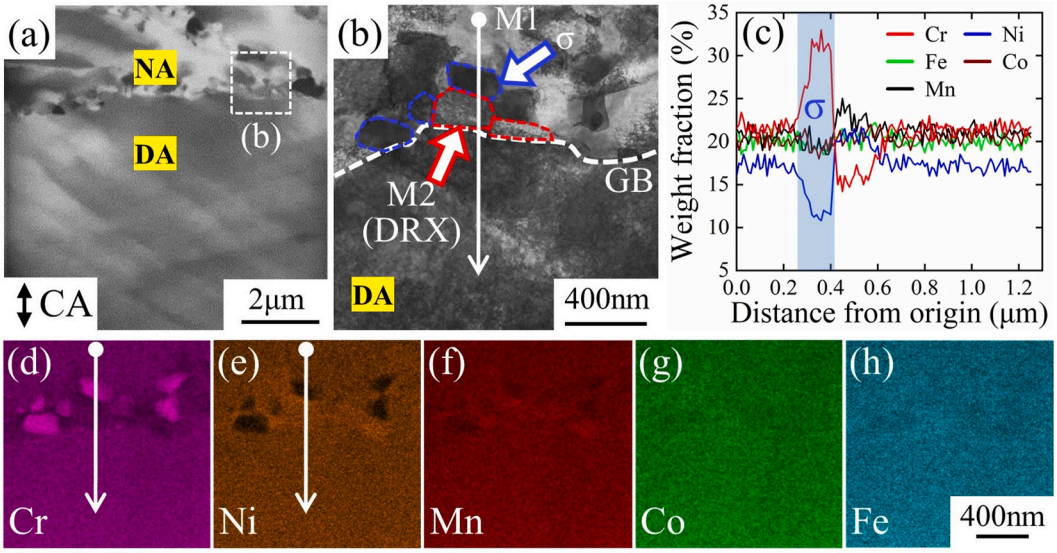

Fig. 3. TEM specimen containing NA and DA prepared by focused ion beam (FIB) milling, as observed via scanning electron microscopy (SEM, a). TEM analysis carried out by scanning transmission electron microscopy (STEM, b). The red circles indicate DRX grains, and the blue circles show the sigma (σ) phases, respectively. The line profile (c) from NA to DA contains the σ and DRX grain (M2), as shown in (b). Energy dispersive spectroscopy (EDS) maps of Cr (d), Ni (e), Mn (f), Co (g), and Fe (h) show the material's chemical distribution for the region of the TEM image (b). (For interpretation of the references to colour in this figure legend, the reader is referred to the Web version of this article.)

partitioning for σ-phase precipitation during hot compression of the CoCrFeMnNi HEA.

2. Experimental procedure

Equiatomic CoCrFeMnNi HEA alloy was prepared and hot deformation was carried out at 700 °C. The alloy was prepared using vacuum induction melting to produce a 60 mm thick ingot (18 kg). For high-temperature rolling, the upper and lower surfaces of the ingot were mechanically polished for 5 mm each to fabricate a 50 mm thick slab. The slab was subjected to a solution treatment at 1150 °C for 2 h and then rolled to a final thickness of 15 mm from 1100 °C to 850 °C, followed by water quenching. Then, it was annealed for 10 min at 1000 °C and water quenched to obtain a fully recrystallized structure. Next, a compression specimen with a height and diameter of 12 mm and 8 mm, respectively, was fabricated.

In the hot deformation at 700 °C, the sample was uniaxially compressed to 70 % at a strain rate of 0.01/s. After compression, the sample was cooled with nitrogen gas to room temperature at an average cooling rate of 30 °C/s. The initial microstructure before compression was a single FCC phase with an average size of approximately 24 μm. The deformed specimen was cut in the compression direction and its center was observed. Microstructure analyses were performed using scanning electron microscopy (SEM), electron backscatter diffraction (EBSD, step size : 0.09 μm), electron channeling contrast imaging (ECCI), and scanning transmission electron microscopy (STEM). Specimens for the EBSD and ECCI analyses were prepared by mechanical polishing followed by electrolytic polishing. For accurate microstructure observation, the target position was prepared via focused ion beam (FIB) milling prior to SEM and STEM observation. For nanoindentation, the surface without etching was measured with a maximum load of 10 mN using a diamond tip. The hardness and elastic modulus were measured with more than five points in the deformed area and necklaced area. EBSD measurement was conducted for the microstructural confirmation after vibratory polishing.

3. Results and discussion

Fig. 1 shows the microstructure represented using EBSD maps after 70 % compression at 700 °C. After compression, the microstructure was divided into a deformed area (DA) in which the initial grains have a pancake shape and a necklaced area (NA) in which fine equiaxed grains developed along the initial grain boundaries. In the NA, the fine equiaxed grains are mainly surrounded by high-angle grain boundaries (HAGBs). Fig. 1b shows an inverse pole figure (IPF) map of the same region as that shown in Fig. 1a, where the crystal orientation is parallel to the compression axis (CA). In the deformed area, the (101) and (001) planes parallel to the CA are mainly observed, whereas the fine equiaxed grains are confirmed to have random texture. In the kernel average misorientation (KAM) map (Fig. 1c), the internal strain of the fine equiaxed grains located at the NA is low, while the strain is relatively higher in the DA. On the other hand, the results of the nanoindentation performed in the DA and NA (Fig. 1d–e) were different, as shown in Fig. 1f–g. It is confirmed that the displacement of NA having low internal strain is smaller than that of DA, which indicates a higher hardness value in NA (Fig. 1f). The average indentation hardness and elastic modulus are shown in Fig. 1g. The hardness and elastic modulus are higher in NA than that of DA, which is opposite to the microstructural tendency identified by EBSD observation. Further analysis at high magnification is necessary for more understanding.

The enlarged interface between NA and DA in Fig. 1 is shown in Fig. 2. The boundary map (Fig. 2a) indicates that fine equiaxed grains with random texture (Fig. 2b) are distributed along the initial grain boundary. This signifies that they are dynamically recrystallized (DRX) grains that are newly generated during the compression. Fig. 2c shows electron channeling contrast imaging (ECCI) in the same region as that for Fig. 2a and b. White σ-phase precipitates (blue arrows) mainly occurred in the NA. High-magnification observation of the boundary between DA and NA (Fig. 2d) shows that the σ-phases occurred around the fine DRX grains. In Fig. 2e, an enlarged DRX grain includes twins, as shown by the red arrows, indicating that the twins appear to be involved in the occurrence of dynamic recrystallization [24–26]. Additionally, it is concluded that the occurrence of σ-precipitates is related to the DRX process because σ-precipitates appear around the DRX grains. In the NA, the internal strain is reduced as DRX grains are generated, but σ-phases are developed around the DRX grains. These phenomena lead to an increase in the hardness and the elastic modulus compared to the DA, as shown in Fig. 1g. The fully recrystallized cantor alloy's elastic modulus

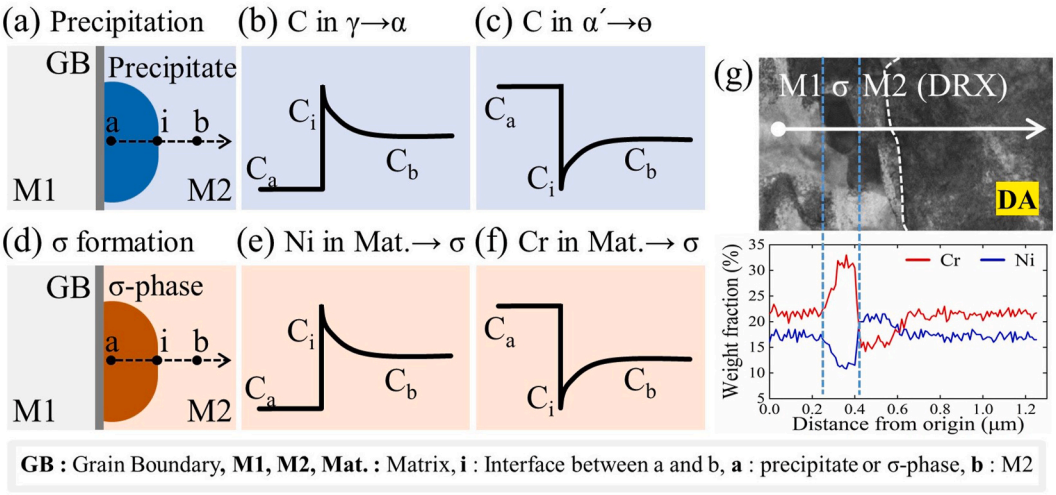

Fig. 4. Illustration of discontinuous precipitation by carbon diffusion (a–c) in carbon steel and σ-phase (σ) formation by Cr and Ni diffusion (d–f) in the present work. TEM image and line profile (g) show the magnified view of the area of Fig. 3 (b).

was 212.62 GPa [27], and the hardness was lower than 2.5 GPa [27,28]. However, higher modulus and hardness were secured by the dislocation in DA and σ-phase in NA generated during compression. The nano-indentation behavior, according to compression and σ-phase conditions, will be discussed in other papers.

TEM observations were conducted to investigate the precipitation behavior of the σ-phase with the results shown in Fig. 3. For the specimen prepared by FIB (Fig. 3a), NA and DA are distinguished, and the region mainly containing NA (white box) was observed using STEM (Fig. 3b). The white dotted line indicates the grain boundary (GB) between DA and NA. The DRX grains (red circles) and σ-phases (blue circles) are shown along with the GB. Line profile analysis (Fig. 3c) was performed from NA to DA, as shown by the solid white lines in Fig. 3b, d, and e. The analysis included the σ-phase and DRX grain. In the line profiles, the σ-phase is Cr-riched and Ni-depleted (Fig. 3c). The concentrations of Fe, Co, and Mn in the σ-phase are the same as in the surrounding matrix. The same region as that shown in the TEM image (Fig. 3b) was EDS-mapped for the contents of Cr, Ni, Mn, Co, and Fe (Fig. 3d–h). As observed from Fig. 3d, Cr is concentrated on the precipitations sized 100-200 nm, as shown in the TEM image (Fig. 3b), whereas Ni is confirmed to have a lower content compared to the matrix. Mn content tends to decrease slightly, while Co and Fe contents do not vary significantly in the EDS mapping. This trend is consistent with the line profile results shown in Fig. 3c, indicating that the σ-phase formation is related to the Cr and Ni diffusion. It is commonly understood that the precipitate formation related to the element diffusion can arise in two cases of the solubility differences.

- Case 1. If the elemental solubility in the precipitate is low, the element migrates to the matrix due to its higher element solubility [29,30].
- Case 2. If the element solubility in the precipitate is high, the precipitate absorbs the element, resulting in its lower concentration in the matrix [30,31].

Here, for the σ-phase, the diffusion of Cr and Ni was also considered based on this approach. This is similar to the diffusion of carbon due to the difference in the carbon solubility of the matrix and the precipitate in carbon steel, which is a well-known phenomenon in physical metallurgy. Fig. 4 schematically shows the diffusion of elements in the above-described two cases for carbon steel (Fig. 4a–c) and for the HEA investigated herein (Fig. 4d–f). Fig. 4a–c shows discontinuous precipitation controlled by carbon diffusion. Fig. 4a shows that when ferrite transformed from the austenite matrix, it precipitates in the austenite GB. Fig. 4b indicates the interface reaction between ferrite (α-phase) and austenite (γ-phase). Carbon diffuses from ferrite (C_a) to austenite (C_b) due to the higher carbon solubility in austenite, showing the behavior of Case 1. In contrast, as shown in Fig. 4c when cementite (ɵ) precipitates in martensite (α´-phase), carbon diffuses from martensite (C_b) to cementite (C_a) due to the higher carbon solubility in cementite, showing the behavior of Case 2. In the precipitate formation at the interface of two grains, the precipitate generally forms either an incoherent interface with the two grains, or a coherent (or semi-coherent) interface with one grain and an incoherent interface with the other grain [30]. The coherent (or semi-coherent) interface has a flat surface, and the incoherent interface has a relatively curved surface with high surface energy due to its elastic strain energy. Therefore, after its formation, the precipitates grow in the direction of the incoherent interface due to its higher surface energy (i to b) (Fig. 4a).

This analytical framework can be applied to understand the dynamic precipitation of σ-phase, as shown in Fig. 4d. In the σ-phase, the solubility of Cr is higher than that of Ni (Fig. 4e and f). Due to the solubility difference between the elements, Ni diffuses to the matrix surrounding the σ-phase as described by Case 1 (Fig. 4e), but Cr is absorbed into the σ-phase following the behavior of Case 2 (Fig. 4f). In addition, the σ-phase grows in the direction of M2 for which the interface is considered to be incoherent (i to b). It is necessary to understand why the interface of the σ-phase migrates in the M2 direction. In Fig. 4g, it is observed that a σ-phase formed between M1 and M2, and line profile analysis was performed from M1 to M2. A sudden change in the concentration in front of the interface between the σ-phase and M2 was observed. Compared to the matrix, Cr concentration decreases, and Ni concentration increases, which is the opposite of the σ-phase behavior. This trend is different from the concentration profile obtained during static precipitation [18,32]. The abrupt change in the concentration occurs due to the interface migration in the M2 direction, indicating that the interface with M2 may be incoherent. In contrast, there is no significant concentration change for M1, indicating that the interface with M1 is likely (semi)coherent.

The σ-phase in the related binary systems such as Cr–Co, Cr–Fe, and Cr–Mn usually exists in a narrow concentration interval. Therefore, it is clear that during the hot compression, the equiatomic CoCrFeMnNi HEA is found in the two-phase area of the FCC matrix and σ-phase of the respective quintenary phase diagram [18], and the σ-phase precipitates from the matrix. Such precipitation of a second phase invariably starts at various boundaries and interfaces. First, nucleation of the precipitate is kinetically easier due to the faster mass transfer along the interfaces compared to mass transfer through the bulk. Second, heterogeneous

Table 1
Precipitation of σ-phase in the equiatomic CoCrFeMnNi high-entropy alloy.

Type	Process	Condition	Composition (σ)	Size (σ)	Reference
Static	Annealing	700 °C for 500 days	46.5Cr-6.6Ni–FeCoMn (at.%)	10–20 μm	Otto et al. [5]
Static	Annealing	700 °C for 500 h	–	2–5 μm	Pickering et al. [23]
Static with REX	HPT and annealing	700 °C for 10 min.	–	100 nm	Park et al. [18]
		700 °C for 60 min.	25Cr–16Ni–FeCoMn (at.%)	100–300 nm	
Dynamic	Hot compression	700 °C, Strain : 70 % Strain rate : 10^{-2}/s	31Cr–11Ni–FeCoMn (wt.%)	100–200 nm	Present work

precipitation is always easier than homogenous precipitation because in homogenous nucleation, a new matrix/σ interface with energy Emat./σ must be formed to "pay" for the formation of spherical precipitate. The energy of this interface is equal to 4πR2Emat./σ where R is the particle radius. For heterogeneous nucleation, the disk of GB with radius R disappears, and the energy cost is lower, namely 4πR2Emat./σ – πR2EGB. This condition is similar to the GB wetting condition but not directly equivalent. Such direct equivalence to the wetting phenomenon would be obtained if instead of being relatively equiaxial, the σ-phase precipitates would have a flat shape elongated along the GB layers. The formation of the Cr-rich σ-phase through the aforementioned phenomenon is further promoted by the strong Cr segregation in the GBs and GB triple junctions [33], and accelerated Cr diffusion along the GB triple junctions [34].

Table 1 shows the data for the precipitation behavior of the σ-phase in the equiatomic CoCrFeMnNi HEA. The σ-phases [5,23] precipitated during the heat treatment of the recrystallized initial structure and the σ-phase [18] associated with the static recrystallization developed by HPT and annealing at 700 °C occur statically. Further precipitation occurred more rapidly and mainly at the grain boundaries, and particularly at the triple junctions. This indicates that the σ-phase was strongly generated when the recrystallization progressed, implying that the recrystallization process is essential for the σ-phase formation in the FCC structure [35,36]. The above results show that the precipitation of the static σ-phase occurs through thermally-driven diffusion, while the recrystallization process during annealing after high deformation interacts with σ-phase nucleation. The movement of defects and elements was activated during the migration of the recrystallized GB and appears to contribute to σ-phase formation. In contrast, herein, the σ-phase dynamically occurs during compression at 700 °C. Compared to the study of Park et al., the compression process has a lower strain (lower accumulated energy) and a shorter period (lower thermal energy). However, the σ-phases in this study tend to be larger and have higher Cr content than that found by Park et al. This indicates that the σ-phase formation is accelerated during the compression. σ-phases occur mainly near interfaces such as high-angle initial grain boundaries, DRX grains, and twins. Particularly, DRX occurs due to the difference in the dislocation density at the crystal interface [37]. In this case, in the moving interface, defects such as pipe diffusion are transferred in large quantities, and thus partitioning of elements such as Cr and Ni is enhanced, as indicated by Fig. 4 and Table 1 [38,39]. The diffusion rate of a moving interface is much higher than that of a static interface [40,41]. These observations suggest that σ-phase kinetics are faster in the dynamic precipitation conditions than in the static conditions.

4. Conclusions

Cr-rich σ-phase in the CoCrFeMnNi HEA dynamically occurred during hot compression at 700 °C. The σ-phase formed around the grain boundaries of the initial and DRX grains leads to the increment of the hardness and elastic modulus. During the formation, Cr was absorbed into the σ-phase, while Ni diffused from the σ-phase. The element partitioning was activated by the moving interface of the DRX grains. Therefore, dynamic precipitation of σ-phase has higher kinetics than that of static precipitation in the CoCrFeMnNi HEA.

CRediT authorship contribution statement

Unhae Lee: Writing - original draft, preparation, Visualization, Investigation. **Boris Straumal:** Writing - review & editing. **Nokeun Park:** Project administration, Conceptualization, Methodology, Writing - review & editing, Submission.

Declaration of competing interest

The authors declare that they have no known competing financial interests or personal relationships that could have appeared to influence the work reported in this paper.

Acknowledgments

This work was supported by the National Research Foundation of Korea (NRF) grant funded by the Korea government (MSIT) (No. NRF-2019R1A2C1088535).

References

[1] B. Cantor, I.T.H. Chang, P. Knight, A.J.B. Vincent, Microstructural development in equiatomic multicomponent alloys, Mater. Sci. Eng. A. 375–377 (2004) 213–218, https://doi.org/10.1016/j.msea.2003.10.257.
[2] J.W. Yeh, Alloy design strategies and future trends in high-entropy alloys, JOM (J. Occup. Med.) 65 (2013) 1759–1771, https://doi.org/10.1007/s11837-013-0761-6.
[3] S. Sohn, Y. Liu, J. Liu, P. Gong, S. Prades-Rodel, A. Blatter, B.E. Scanley, C. C. Broadbridge, J. Schroers, Noble metal high entropy alloys, Scripta Mater. 126 (2017) 29–32, https://doi.org/10.1016/j.scriptamat.2016.08.017.
[4] B. Schuh, F. Mendez-Martin, B. Völker, E.P. George, H. Clemens, R. Pippan, A. Hohenwarter, Mechanical properties, microstructure and thermal stability of a nanocrystalline CoCrFeMnNi high-entropy alloy after severe plastic deformation, Acta Mater. 96 (2015) 258–268, https://doi.org/10.1016/j.actamat.2015.06.025.
[5] F. Otto, A. Dlouhý, K.G. Pradeep, M. Kuběnová, D. Raabe, G. Eggeler, E.P. George, Decomposition of the single-phase high-entropy alloy CrMnFeCoNi after prolonged anneals at intermediate temperatures, Acta Mater. 112 (2016) 40–52, https://doi.org/10.1016/j.actamat.2016.04.005.
[6] F. Otto, A. Dlouhý, C. Somsen, H. Bei, G. Eggeler, E.P. George, The influences of temperature and microstructure on the tensile properties of a CoCrFeMnNi high-entropy alloy, Acta Mater. 61 (2013) 5743–5755, https://doi.org/10.1016/j.actamat.2013.06.018.
[7] A. Gali, E.P. George, Tensile properties of high- and medium-entropy alloys, Intermetallics 39 (2013) 74–78, https://doi.org/10.1016/j.intermet.2013.03.018.
[8] A. Haglund, M. Koehler, D. Catoor, E.P. George, V. Keppens, Polycrystalline elastic moduli of a high-entropy alloy at cryogenic temperatures, Intermetallics 58 (2015) 62–64, https://doi.org/10.1016/j.intermet.2014.11.005.
[9] Z. Wu, H. Bei, G.M. Pharr, E.P. George, Temperature dependence of the mechanical properties of equiatomic solid solution alloys with face-centered cubic crystal structures, Acta Mater. 81 (2014) 428–441, https://doi.org/10.1016/j.actamat.2014.08.026.
[10] B. Gludovatz, A. Hohenwarter, D. Catoor, E.H. Chang, E.P. George, R.O. Ritchie, A fracture-resistant high-entropy alloy for cryogenic applications, Science 345 (80) (2014) 1153–1158, https://doi.org/10.1126/science.1254581.
[11] S.S. Sohn, A. Kwiatkowski da Silva, Y. Ikeda, F. Körmann, W. Lu, W.S. Choi, B. Gault, D. Ponge, J. Neugebauer, D. Raabe, Ultrastrong medium-entropy single-phase alloys designed via severe lattice distortion, Adv. Mater. 31 (2019) 1807142, https://doi.org/10.1002/adma.201807142.
[12] G. Qin, W. Xue, R. Chen, H. Zheng, L. Wang, Y. Su, H. Ding, J. Guo, H. Fu, Grain refinement and FCC phase formation in AlCoCrFeNi high entropy alloys by the addition of carbon, Materialia 6 (2019) 100259, https://doi.org/10.1016/j.mtla.2019.100259.
[13] T.A. Listyawan, H. Lee, N. Park, U. Lee, Microstructure and mechanical properties of CoCrFeMnNi high entropy alloy with ultrasonic nanocrystal surface modification process, J. Mater. Sci. Technol. 57 (2020) 123–130, https://doi.org/10.1016/j.jmst.2020.02.083.

[14] M. Choi, I. Ondicho, N. Park, N. Tsuji, Strength–ductility balance in an ultrafine-grained non-equiatomic Fe50(CoCrMnNi)50 medium-entropy alloy with a fully recrystallized microstructure, J. Alloys Compd. 780 (2019) 959–966, https://doi.org/10.1016/j.jallcom.2018.11.265.
[15] F. Otto, N.L. Hanold, E.P. George, Microstructural evolution after thermomechanical processing in an equiatomic, single-phase CoCrFeMnNi high-entropy alloy with special focus on twin boundaries, Intermetallics 54 (2014) 39–48, https://doi.org/10.1016/j.intermet.2014.05.014.
[16] P.P. Bhattacharjee, G.D. Sathiaraj, M. Zaid, J.R. Gatti, C. Lee, C.-W. Tsai, J.-W. Yeh, Microstructure and texture evolution during annealing of equiatomic CoCrFeMnNi high-entropy alloy, J. Alloys Compd. 587 (2014) 544–552, https://doi.org/10.1016/j.jallcom.2013.10.237.
[17] K.-H. Lin, S.-Y. Chang, Y.-C. Lo, C.-C. Wang, S.-J. Lin, J.-W. Yeh, Differences in texture evolution from low-entropy to high-entropy face-centered cubic alloys during tension test, Intermetallics 118 (2020) 106635, https://doi.org/10.1016/j.intermet.2019.106635.
[18] N. Park, B.J. Lee, N. Tsuji, The phase stability of equiatomic CoCrFeMnNi high-entropy alloy: comparison between experiment and calculation results, J. Alloys Compd. 719 (2017) 189–193, https://doi.org/10.1016/j.jallcom.2017.05.175.
[19] Z.H. Zhu, W.D. Zhang, X.H. Tu, X.J. Wang, W. Li, Effect of sigma phase precipitation on microstructure and properties of cast ZG0Cr26Ni5Mo3Cu3 duplex stainless steel under different heat treatments, China Foundry 15 (2018) 182–188, https://doi.org/10.1007/s41230-018-7226-z.
[20] S.S.M. Tavares, J.A. de Souza, L.F.G. Herculano, H.F.G. de Abreu, C.M. de Souza, Microstructural, magnetic and mechanical property changes in an AISI 444 stainless steel aged in the 560 °C to 800 °C range, Mater. Char. 59 (2008) 112–116, https://doi.org/10.1016/j.matchar.2006.11.002.
[21] A.F. Padilha, P.R. Rios, Decomposition of austenite in austenitic stainless steels, ISIJ Int. 42 (2002) 325–337, https://doi.org/10.2355/isijinternational.42.325.
[22] Y.H. Jo, W.M. Choi, D.G. Kim, A. Zargaran, K. Lee, H. Sung, S.S. Sohn, H.S. Kim, B. J. Lee, S. Lee, Utilization of brittle σ phase for strengthening and strain hardening in ductile VCrFeNi high-entropy alloy, Mater. Sci. Eng. A. 743 (2019) 665–674, https://doi.org/10.1016/j.msea.2018.11.136.
[23] E.J. Pickering, R. Muñoz-Moreno, H.J. Stone, N.G. Jones, Precipitation in the equiatomic high-entropy alloy CrMnFeCoNi, Scripta Mater. 113 (2016) 106–109, https://doi.org/10.1016/j.scriptamat.2015.10.025.
[24] J. Li, B. Gao, S. Tang, B. Liu, Y. Liu, Y.T. Wang, J. Wang, High temperature deformation behavior of carbon-containing FeCoCrNiMn high entropy alloy, J. Alloys Compd. 747 (2018) 571–579, https://doi.org/10.1016/j.jallcom.2018.02.332.
[25] R.R. Eleti, T. Bhattacharjee, L. Zhao, P.P. Bhattacharjee, N. Tsuji, Hot deformation behavior of CoCrFeMnNi FCC high entropy alloy, Mater. Chem. Phys. 210 (2018) 176–186, https://doi.org/10.1016/j.matchemphys.2017.06.062.
[26] N.D. Stepanov, D.G. Shaysultanov, N.Y. Yurchenko, S.V. Zherebtsov, A.N. Ladygin, G.A. Salishchev, M.A. Tikhonovsky, High temperature deformation behavior and dynamic recrystallization in CoCrFeNiMn high entropy alloy, Mater. Sci. Eng. A. 636 (2015) 188–195, https://doi.org/10.1016/j.msea.2015.03.097.
[27] D. Wu, J.S.C. Jang, T.G. Nieh, Elastic and plastic deformations in a high entropy alloy investigated using a nanoindentation method, Intermetallics 68 (2016) 118–127, https://doi.org/10.1016/j.intermet.2015.10.002.
[28] S. Sinha, R.A. Mirshams, T. Wang, S.S. Nene, M. Frank, K. Liu, R.S. Mishra, Nanoindentation behavior of high entropy alloys with transformation-induced plasticity, Sci. Rep. 9 (2019) 6639, https://doi.org/10.1038/s41598-019-43174-x.
[29] H.K.D.H. Bhadeshia, Diffusional formation of ferrite in iron and its alloys, Prog. Mater. Sci. 29 (1985) 321–386, https://doi.org/10.1016/0079-6425(85)90004-0.
[30] D.A. Porter, K.E. Easterling, Phase Transformations in Metals and Alloys, second ed., Springer US, Boston, MA, 1992 https://doi.org/10.1007/978-1-4899-3051-4.
[31] M. Enomoto, K. Hayashi, Modeling the growth of austenite in association with cementite during continuous heating in low-carbon martensite, J. Mater. Sci. 53 (2018) 6911–6921, https://doi.org/10.1007/s10853-018-2020-2.
[32] G. Laplanche, S. Berglund, C. Reinhart, A. Kostka, F. Fox, E.P. George, Phase stability and kinetics of σ-phase precipitation in CrMnFeCoNi high-entropy alloys, Acta Mater. 161 (2018) 338–351, https://doi.org/10.1016/j.actamat.2018.09.040.
[33] P. Stender, Z. Balogh, G. Schmitz, Triple junction segregation in nanocrystalline multilayers, Phys. Rev. B 83 (2011) 121407, https://doi.org/10.1103/PhysRevB.83.121407.
[34] P. Stender, Z. Balogh, G. Schmitz, Triple line diffusion in nanocrystalline Fe/Cr and its impact on thermal stability, Ultramicroscopy 111 (2011) 524–529, https://doi.org/10.1016/j.ultramic.2010.10.021.
[35] F. Abe, H. Araki, T. Noda, Discontinuous precipitation of σ-phase during recrystallisation in cold rolled Fe–10Cr–30Mn austenite, Mater. Sci. Technol. 4 (1988) 885–893, https://doi.org/10.1179/mst.1988.4.10.885.
[36] E. Hornbogen, Inhibition of recrystallization in supersaturated solid solutions by large amounts of cold work, J. Mater. Sci. 12 (1977) 1565–1572, https://doi.org/10.1007/BF00542807.
[37] A. Rollett, F. Humphreys, G.S. Rohrer, M. Hatherly, Recrystallization and Related Annealing Phenomena, Second Ed, second ed., Recryst. Relat. Annealing Phenom, 2004 https://doi.org/10.1016/B978-0-08-044164-1.X5000-2, 1–628.
[38] A. Deschamps, G. Fribourg, Y. Bréchet, J.L. Chemin, C.R. Hutchinson, In situ evaluation of dynamic precipitation during plastic straining of an Al–Zn–Mg–Cu alloy, Acta Mater. 60 (2012) 1905–1916, https://doi.org/10.1016/j.actamat.2012.01.002.
[39] J.M. Vitek, S.A. David, Sigma phase transformation in austenitic stainless steels, Weld. J. (Miami, Fla) 65 (1986) 106s–111s.
[40] K. Smidoda, W. Gottschalk, H. Gleiter, Diffusion in migrating interfaces, Acta Metall. 26 (1978) 1833–1836, https://doi.org/10.1016/0001-6160(78)90095-0.
[41] K. Smidoda, C. Gottschalk, H. Gleiter, Grain boundary diffusion in migrating boundaries, Met. Sci. 13 (1979) 146–148, https://doi.org/10.1179/msc.1979.13.3-4.146.